

Cahn-Hilliard/Navier-Stokes model for the simulation of three-phase flows

F. Boyer, C. Lapuerta, S. Minjeaud, B. Piar
and M. Quintard

Received: date / Accepted: date

Abstract In this paper, we describe some aspects of the diffuse interface modelling of incompressible flows, composed of three immiscible components, without phase change. In the diffuse interface methods, the system evolution is driven by the minimisation of a free energy. The originality of our approach, derived from the Cahn-Hilliard model, comes from the particular form of the energy we proposed in [4], which, among other interesting properties, ensures consistency with the two-phase model.

The modelling of three-phase flows is further completed by coupling the Cahn-Hilliard system and the Navier-Stokes equations where surface tensions are taken into account through volumic capillary forces.

These equations are discretized in time and space paying attention to the fact that most of the main properties of the original model (volume conservation, energy estimate) have to be maintained at the discrete level. An adaptive refinement method is finally used to obtain an accurate resolution of very thin moving internal layers, while limiting the total number of cells in the grids all along the simulation.

Different numerical results are given, from the validation case of the lens spreading between two phases (contact angles, pressure jumps), to the study of mass transfer through a liquid/liquid interface crossed by a single rising gaz bubble. The numerical applications are performed with large ratio between densities and viscosities and three different surface tensions.

Keywords Cahn-Hilliard/Navier-Stokes model · three phase flows · local adaptive refinement

F. Boyer
Université Paul Cézanne, Avenue Escadrille Normandie-Niemen, 13397 MARSEILLE Cedex
20 FRANCE
E-mail: fboyer@latp.univ-mrs.fr

C. Lapuerta, S. Minjeaud and B. Piar
Institut de Radioprotection et de Sûreté Nucléaire, Bat 702, BP3, 13115 Saint Paul lez Durance,
FRANCE
E-mail: celine.lapuerta,sebastian.minjeaud,bruno.piar@irsn.fr

M. Quintard
Institut de Mécanique des Fluides de Toulouse, Allée du Professeur Camille Soula, 31400
TOULOUSE, FRANCE
E-mail: Michel.Quintard@imft.fr

1 Introduction

Three-phase flows are very important in many applications, within or outside porous media (nuclear safety, petroleum engineering,...). Direct simulations with diffuse interface models (see for instance the review in [1]) in the case of two-phase flows have proven to be very useful to answer fundamental questions concerning the different occurring mechanisms (see for examples [2,7,22]). Unfortunately, few numerical models are available to directly simulate three-phase flows. We can note the works of Kim and co. which have studied how to generalize the coupling between such multi-component Cahn-Hilliard models and the Navier-Stokes equations and how to implement efficient numerical solvers (see [17,15,16]).

In this paper, we propose a diffuse interface modelling based on the Cahn-Hilliard approach for the study of incompressible flows, composed of three immiscible components. The construction of a free energy which has good properties is crucial to obtain a model able to simulate both two- and three- phase situations. Our approach ensures that there is no artificial apparition of one phase inside the interface between the other two. In order to describe the hydrodynamics of the mixture, the Cahn-Hilliard and the Navier-Stokes equations for incompressible flows are coupled. The interfacial surface tension forces are naturally taken into account through volumic capillary forces. The details of the construction and the analysis of the three component Cahn-Hilliard model are given in [4].

A numerical difficulty for the Cahn-Hilliard approach is to have an accurate resolution of very thin moving internal layers. To address this question, we choose to use a refinement method called CHARMS (Conforming Hierarchical Adaptive Refinement MethodS), initially developed by Krysl, Grinspun, Schröder in [18]. The key feature of the method is to perform basis functions (un-)refinement instead of cells (un-)refinement.

The outline of the paper is the following. In Section 2, after a brief introduction to the usual binary Cahn-Hilliard model, we present the general construction of a ternary model. The next section is devoted to the numerical schemes for the Cahn-Hilliard/Navier-Stokes system using the local adaptive refinement method. Finally, in the last section, two applications are presented: the partial and total spreading of the lens between two liquids and the gaz bubble rising through two stratified fluid layers.

2 Three component Cahn-Hilliard/Navier-Stokes model

In this section, we propose a general description of the ternary Cahn-Hilliard/Navier-Stokes model. The complete derivation and the analysis of the model are given in [4].

2.1 Introduction: Cahn-Hilliard model

The Cahn-Hilliard approach consists in assuming that the interface thickness between two phases in the system is small but greater than the real physical one. One phase is described geometrically by a smooth function c_i , called "order parameter", which is equal to 1 in the phase i and 0 outside, and which varies continuously in the interfaces between the phase i and the others (Figure 1).

The system evolution is driven by the minimisation of a free energy. The two-component Cahn-Hilliard free energy is defined by

$$\mathcal{F}_{\sigma,\varepsilon}^{\text{diph}}(c) = \int_{\Omega} \left[\frac{12}{\varepsilon} F(c) + \frac{3}{4} \sigma \varepsilon |\nabla c|^2 \right], \quad (1)$$

with $F(c) = \sigma c^2(1-c)^2$. The first term is called ‘‘bulk energy’’ and the function F , called the Cahn-Hilliard potential, has a classical double-well structure with two minima for $c = 0$ and $c = 1$ (Figure 1) corresponding to the two pure phases. This energy tends to reduce the interfacial zone width whereas the second term $|\nabla c|^2$, called capillary term, tends to increase it. In this definition, σ is the surface tension and ε is the interface thickness. From a numerical point of view, one of the main features of this model is that ε can be chosen larger than its theoretical value without modifying the capillary properties of the interfaces.

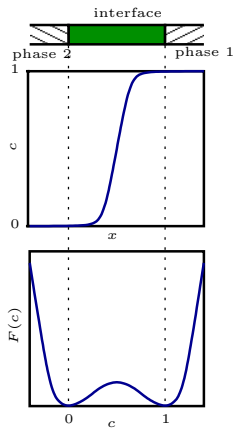


Fig. 1 Variation of the order parameter between two phases and double-well structure of the Cahn-Hilliard potential F

The evolution of the order parameter is driven by the gradient of the functional derivative $\mu = \frac{\delta \mathcal{F}_{\sigma,\varepsilon}^{\text{diph}}}{\delta c}$, called generalised chemical potential:

$$\begin{cases} \frac{\partial c}{\partial t} - \nabla \cdot (M_0 \nabla \mu) = 0, \\ \mu = \frac{\delta \mathcal{F}_{\sigma,\varepsilon}^{\text{diph}}}{\delta c} = -\frac{3}{2} \sigma \varepsilon \Delta c + 24 \frac{\sigma}{\varepsilon} c(1-c)(1-2c). \end{cases} \quad (2)$$

The parameter M_0 , called the mobility, is a diffusion coefficient which may depend on c . The boundary conditions are in general the homogeneous Neumann boundary conditions. For the potential μ , this condition ensures that there is no mass diffusion through the boundary. For the order parameter c , this condition implies that the interfaces are supposed to be orthogonal to the boundary of the computational domain. One interesting feature of Cahn-Hilliard models is that it is possible to consider non-homogeneous and non-linear Neumann conditions to model more general contact angles.

2.2 Construction of a three-component model

Our aim is to generalise the diphasic Cahn-Hilliard models presented above for the simulation of three immiscible component flows. We introduce three order parameters c_1 , c_2 and c_3 , each representing the "concentration" of one component. Moreover, we want that the three-phase model satisfies the following physical constraints:

1. $\sum_{i=1}^3 c_i = 1$ for each point and each time (perfect mixture),
2. the equations satisfied by c_1 , c_2 and c_3 should be formally identical,
3. the three phase model should coincide with the two phase model when only two phases are present.

Remark 1 In particular, one of the order parameters c_1 , c_2 or c_3 will be eliminated *a posteriori* and the solution must not depend on the choice of the eliminated unknown. Only two coupled Cahn-Hilliard equations will be solved for practical reasons.

2.2.1 Free energy and evolution equations

In view of the diphasic case, we postulate that the free energy can be written as follows

$$\mathcal{F}_{\Sigma, \varepsilon}^{\text{triph}}(c_1, c_2, c_3) = \int_{\Omega} \left[\frac{12}{\varepsilon} F(c_1, c_2, c_3) + \frac{3}{8} \varepsilon \Sigma_1 |\nabla c_1|^2 + \frac{3}{8} \varepsilon \Sigma_2 |\nabla c_2|^2 + \frac{3}{8} \varepsilon \Sigma_3 |\nabla c_3|^2 \right], \quad (3)$$

with a bulk energy F and three capillary terms.

The coefficients Σ_1 , Σ_2 , Σ_3 and the function F will be determined later and we first concentrate here on the evolution equations associated to this model, taking into account the constraint

$$\sum_{i=1}^3 c_i = 1. \quad (4)$$

As in the diphasic case, the evolution of the order parameters is driven by the minimisation of the free energy. In order to ensure the constraint (4), a Lagrange multiplier technique is used. The Cahn-Hilliard equations we finally obtain are

$$\forall i \in \{1, 2, 3\}, \quad \begin{cases} \frac{\partial c_i}{\partial t} = \nabla \cdot \left(\frac{M_0}{\Sigma_i} \nabla \mu_i \right), \\ \mu_i = \frac{4\Sigma_T}{\varepsilon} \sum_{j \neq i} \left(\frac{1}{\Sigma_j} (\partial_i F(\mathbf{c}) - \partial_j F(\mathbf{c})) \right) - \frac{3}{4} \varepsilon \Sigma_i \Delta c_i, \end{cases} \quad (5)$$

where the coefficient Σ_T is defined by $\frac{3}{\Sigma_T} = \frac{1}{\Sigma_1} + \frac{1}{\Sigma_2} + \frac{1}{\Sigma_3}$. The details of the derivation of these equations are given in [4].

2.2.2 Consistency with the two-phase model

In order to ensure the physical constraints described above, the model must satisfy two properties :

- (1) When a phase i is not present, the three-phase free energy is equal to the one of the two-phase model,

- (2) When a phase i is not present at initial time, the phase must not appear artificially during the evolution of the system.

In this case, we say that the model is *algebraically consistent* with the two-phase models (see [4]).

Capillary terms: In order to satisfy the property (1), we easily find that the capillary coefficients have to be taken as follows

$$\Sigma_i = \sigma_{ij} + \sigma_{ik} - \sigma_{jk}, \quad (6)$$

where the surface tensions σ_{12} , σ_{13} and σ_{23} are given.

The coefficient $S_i = -\Sigma_i$ is called spreading parameter of the phase i at the interface between phases j and k [21]. If S_i is positive, the spreading is said to be total and if S_i is negative, it is said to be partial (see Section 4.1). It is interesting to notice here, and this will be enforced by the discussion in the sequel of the paper, that the spreading coefficient appears as a key parameter in the proposed Cahn-Hilliard formulation. Indeed, there is an extensive literature that shows the importance of this parameter in the case of three-phase flow, especially for flow in porous media (see [13, 19]).

Bulk energy: In view of the diphasic case, a natural bulk energy would be

$$\bar{F} = \sigma_{12}c_1^2c_2^2 + \sigma_{13}c_1^2c_3^2 + \sigma_{23}c_2^2c_3^2. \quad (7)$$

Unfortunately, this function does not ensure the algebraic consistency.

To understand this, we propose to visualise the map of the function \bar{F} in barycentric coordinates (see Figure 2). More precisely, we represent the Gibbs triangle where the vertices correspond to the three pure phases. The points located at the interior of the triangle represents physically admissible values of the concentration. We observe inside the triangle a local minimum of \bar{F} . Since the evolution of the system is driven by the minimisation of the total energy, the choice of \bar{F} will lead to non-physical apparition of one phase in the interface between the other two. Indeed, the least energy path between two vertices i, j (corresponding two pure phases) goes into the interior of the triangle since there is a local minimum. In the numerical application in the following Part 2.2.3, we observe this behaviour.

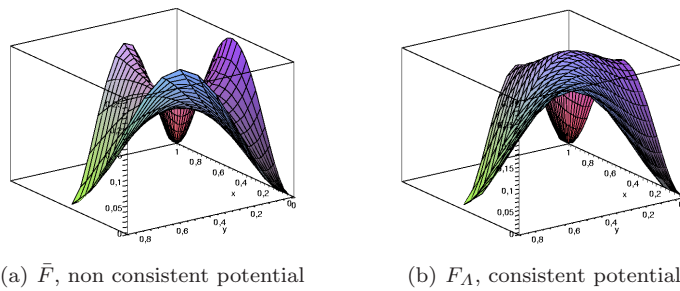


Fig. 2 Surfaces defined by \bar{F} and F_A in barycentric coordinates

In [4], we show that, instead of \bar{F} , using the Cahn-Hilliard potential defined by

$$F_\Lambda = \sigma_{12}c_1^2c_2^2 + \sigma_{13}c_1^2c_3^2 + \sigma_{23}c_2^2c_3^2 + c_1c_2c_3(\Sigma_1c_1 + \Sigma_2c_2 + \Sigma_3c_3) + \Lambda c_1^2c_2^2c_3^2 \quad (8)$$

for $\Lambda > 0$ large enough, ensures the algebraic consistency property. In Figure 2, we see that the function has no minimum in the Gibbs triangle and that, the least energy path between two vertices, is exactly described by the corresponding edge of the triangle.

In practice, we note $F_\Lambda = F_0 + P$ where

$$\begin{aligned} F_0 &= \sigma_{12}c_1^2c_2^2 + \sigma_{13}c_1^2c_3^2 + \sigma_{23}c_2^2c_3^2 + c_1c_2c_3(\Sigma_1c_1 + \Sigma_2c_2 + \Sigma_3c_3), \\ P &= \Lambda c_1^2c_2^2c_3^2. \end{aligned} \quad (9)$$

Properties: The analysis of the consistent model is given in [4]. In particular, we show that, in order to prove the well-posedness of the system, it is needed to assume that the following conditions hold

$$\begin{cases} \Sigma_1\Sigma_2 + \Sigma_1\Sigma_3 + \Sigma_2\Sigma_3 > 0, \\ \Sigma_i + \Sigma_j > 0 \text{ for } i \neq j. \end{cases} \quad (10)$$

Notice that the second condition is always satisfied because, from (6), we deduce that

$$\Sigma_i + \Sigma_j = 2\sigma_{ij} > 0. \quad (11)$$

Moreover, the only condition on the sign of the coefficients Σ_i is the first equation in (10). In particular, the model is able to take into account total spreading situations (see Paragraph 4.1) provided that $\Lambda > 0$ is chosen large enough. In other situations (all coefficients $\Sigma_i > 0$), one can take $\Lambda = 0$.

2.2.3 Numerical example: consistent/non-consistent model

To compare the consistent and non-consistent models, we used the classical problem of the simulation of the partial spreading of a liquid lens between two other liquid phases. At the equilibrium, the shape of the lens and the contact angles are well known (Young's relation). This example is studied in details in Section 4.1.

For three different surface tensions

$$\begin{aligned} \sigma_{\text{upper/lens}} &= 0.8, \\ \sigma_{\text{lower/lens}} &= 1.4, \\ \sigma_{\text{lower/upper}} &= 1, \end{aligned}$$

the numerical solution for the consistent model ($F = F_\Lambda$) is given in Figure 3.

In Figure 4, we visualise the order parameter associated to the lower liquid phase. When we use the non-consistent model ($F = \bar{F}$) we observe that the lower phase appears artificially in the interface between the upper phase and the lens. This unsatisfactory behaviour is no more present when we use the potential $F = F_\Lambda$.

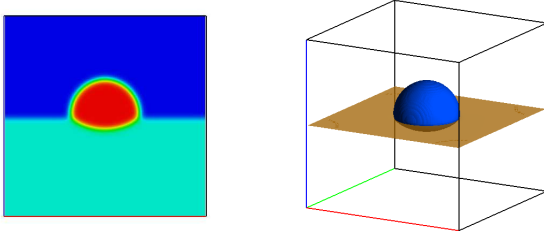
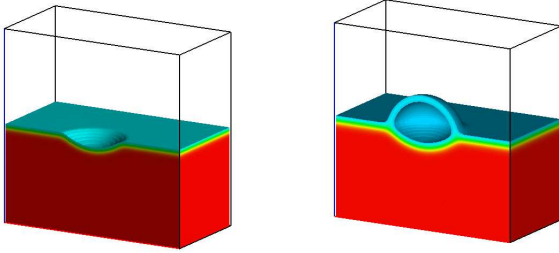


Fig. 3 Partial spreading of a lens between two stratified liquids



(a) consistent model $F = F_A$ (b) non-consistent model $F = \bar{F}$

Fig. 4 Lower phase for consistent/non-consistent model

2.3 Coupling with the hydrodynamics

To complete the modelling of three-phase incompressible flows, the Cahn-Hilliard system (5) is then coupled with Navier-Stokes equations (for more details see [3, 4, 11, 14]).

The velocity jump being zero between two phases, it is possible to define a unique velocity field which is smooth on the domain. In order to couple the equations, a convective term is added in the order parameters evolution equations and a capillary force,

$$F_{ca} = \mu_1 \nabla c_1 + \mu_2 \nabla c_2 + \mu_3 \nabla c_3, \quad (12)$$

is considered in the momentum balance. This force is a volumic approximation of the surface tension force (see [14]). To this end, the Navier-Stokes equations are written as follows

$$\begin{cases} \sqrt{\varrho} \frac{\partial}{\partial t} (\sqrt{\varrho} \mathbf{u}) + (\varrho \mathbf{u} \cdot \nabla) \mathbf{u} + \frac{\mathbf{u}}{2} \nabla \cdot (\varrho \mathbf{u}) - \nabla \cdot (\eta (\nabla \mathbf{u} + \nabla \mathbf{u}^t)) + \nabla p = \varrho \mathbf{g} + F_{ca}, \\ \nabla \cdot \mathbf{u} = 0, \end{cases} \quad (13)$$

where the density ϱ and the viscosity η are smooth functions which depend on the order parameters and satisfy, in the i -phase,

$$\varrho = \varrho_i, \quad \eta = \eta_i, \quad (14)$$

(details are given in Section 3.1).

Remark 2 In this formulation, the free energy creation by convection is balanced with the kinetic energy creation by capillarity (see [4,11]).

This Navier-Stokes formulation would be equivalent with the classical form if one uses the usual mass balance equation $\frac{\partial}{\partial t}\rho + \nabla \cdot (\rho \mathbf{u}) = 0$. However, in the diffuse interface modelling framework, the mass balance equation has a slightly different form since ρ depends on c_1, c_2, c_3 which have their own evolution equation. In practice, the mass balance equation possesses an additional diffusion term (which comes from diffusion terms of (5)). Hence, the above formulation of the Navier-Stokes equations is strictly equivalent neither to the conservative formulation nor to the non-conservative formulation.

The reason for the choice of this formulation, initially proposed by Guermond and Quartapelle [10] in the more usual context of variable-density incompressible single phase flows, is that it guarantees the control of the kinetic energy even if the mass balance equation has not the classical form. Indeed, multiplying the momentum equation by \mathbf{u} and integrating on the domain, the time derivative form enables to obtain the time derivative kinetic energy

$$\int_{\Omega} \frac{\partial}{\partial t} (\sqrt{\rho} \mathbf{u}) \cdot \sqrt{\rho} \mathbf{u} = \frac{1}{2} \frac{d}{dt} \int_{\Omega} \rho \mathbf{u}^2. \quad (15)$$

Furthermore, the convective contribution is zero

$$\int_{\Omega} \left[\mathbf{u} \cdot (\rho \mathbf{u} \cdot \nabla) \mathbf{u} + \frac{\mathbf{u}^2}{2} \nabla \cdot (\rho \mathbf{u}) \right] = 0. \quad (16)$$

Indeed, assuming that $\mathbf{u} = 0$ on the boundary of the domain, then for any scalar function f , we have

$$\int_{\Omega} f (\rho \mathbf{u} \cdot \nabla) f + \int_{\Omega} \frac{f^2}{2} \nabla \cdot (\rho \mathbf{u}) = \frac{1}{2} \int_{\Omega} \nabla \cdot (\rho \mathbf{u} f^2) = \frac{1}{2} \int_{\partial \Omega} \rho f^2 \mathbf{u} \cdot \mathbf{n} = 0. \quad (17)$$

In the Navier-Stokes equations, we use this calculation for each velocity component. The other terms in the equations (13) are written under a standard form.

3 Numerical methods

A numerical issue in using the Cahn-Hilliard approach is to ensure accuracy of the resolution of very thin moving internal layers while limiting the total number of cells in the grid and thus the computational cost. The solution adopted here is the use of a local adaptive refinement method (CHARMS) proposed by Krysl, Grinspun and Schröder [18].

In this section, we give the time and spatial discretizations for the Cahn-Hilliard and Navier-Stokes (CH/NS) system which ensures that the discrete total energy (the sum of the Cahn-Hilliard free energy and the kinetic energy) are controlled, at least for a time step small enough. Then, we propose a brief description of the CHARMS method and of its use for our applications.

The practical implementation has been performed using the software object-oriented component library PELICANS [20], developed at the french "Institut de Radioprotection et de Sûreté Nucléaire" (IRSN) and distributed under the CeCILL-C license agreement (an adaptation of LGPL to the French law).

3.1 Time and space discretizations

In order to solve the CH/NS system, we use a Galerkin finite element method. The time discretization used is semi-implicit in order to split the Cahn-Hilliard and the Navier-Stokes problems within a time step as explained below. The resolution is performed using a Newton-Raphson method for the Cahn-Hilliard system and an Augmented Lagrangian method for Navier-Stokes equations.

Noting \mathcal{V}_x the finite element approximation space where we seek the discrete unknown x , the time marching in a time step is written as follows:

Let $c_i^n, \mu_i^n, \mathbf{u}^n$ be known for $i = 1, 2$,

1. find $(c_1^{n+1}, c_2^{n+1}, \mu_1^{n+1}, \mu_2^{n+1}) \in (\mathcal{V}_{c,\mu})^4$ such that $\forall \nu \in \mathcal{V}_{c,\mu}$, we have for $i = 1, 2$

$$\int_{\Omega} \frac{c_i^{n+1} - c_i^n}{\Delta t} \nu + \int_{\Omega} \frac{M_0^n}{\Sigma_i} \nabla \mu_i^{n+1} \cdot \nabla \nu + \int_{\Omega} \mathbf{u}^n \cdot \nabla c_i^{n+1} \nu = 0, \quad (18)$$

$$\int_{\Omega} \mu_i^{n+1} \nu = \int_{\Omega} D_i(\mathbf{c}^{n+1}, \mathbf{c}^n) \nu + \int_{\Omega} \frac{3}{4} \Sigma_i \varepsilon \nabla c_i^{n+1} \cdot \nabla \nu. \quad (19)$$

with $D_i(\mathbf{c}^{n+1}, \mathbf{c}^n) = \frac{4\Sigma_T}{\varepsilon} \sum_{j \neq i} \left(\frac{1}{\Sigma_j} (d_i(\mathbf{c}^{n+1}, \mathbf{c}^n) - d_j(\mathbf{c}^{n+1}, \mathbf{c}^n)) \right)$ where d_i represents a semi-implicit discretization of $\partial_{c_i} F_A$ defined by

$$d_i(\mathbf{c}^{n+1}, \mathbf{c}^n) = \partial_i F_0(\mathbf{c}^{n+1}) + \frac{2}{3} A c_i^{n+1} \left[(c_j^n)^2 (c_k^n)^2 + \frac{1}{2} (c_j^{n+1})^2 (c_k^n)^2 + \frac{1}{2} (c_j^n)^2 (c_k^{n+1})^2 + (c_j^{n+1})^2 (c_k^{n+1})^2 \right]. \quad (20)$$

2. Using c_i^{n+1} and μ_i^{n+1} ($i = 1, 2$), compute $c_3^{n+1}, \mu_3^{n+1}, F_{ca}^{n+1} = \sum_{i=1}^3 \mu_i^{n+1} \nabla c_i^{n+1}$, ϱ^{n+1} and η^{n+1} .
3. Find $\mathbf{u}^{n+1} \in \mathcal{V}_u$ and $p^{n+1} \in \mathcal{V}_p$ such that $\forall \mathbf{v} \in \mathcal{V}_u$ and $\forall q \in \mathcal{V}_p$

$$\begin{aligned} \int_{\Omega} \sqrt{\varrho^{n+1}} \frac{\sqrt{\varrho^{n+1}} \mathbf{u}^{n+1} - \sqrt{\varrho^n} \mathbf{u}^n}{\Delta t} \cdot \mathbf{v} + \int_{\Omega} 2\eta^{n+1} D(\mathbf{u}^{n+1}) : \nabla \mathbf{v} \\ + \frac{1}{2} \int_{\Omega} (\varrho^{n+1} (\mathbf{u}^n \cdot \nabla) \mathbf{u}^{n+1}) \cdot \mathbf{v} - \frac{1}{2} \int_{\Omega} (\varrho^{n+1} (\mathbf{u}^n \cdot \nabla) \mathbf{v}) \cdot \mathbf{u}^{n+1} \\ = \int_{\Omega} p^{n+1} \nabla \cdot \mathbf{v} + \int_{\Omega} (F_{ca}^{n+1} + \varrho^{n+1} g) \cdot \mathbf{v}, \end{aligned} \quad (21)$$

$$\int_{\Omega} \nabla \cdot \mathbf{u}^{n+1} q = 0. \quad (22)$$

In (19), the time discretization, $D_i(\mathbf{c}^{n+1}, \mathbf{c}^n)$, of the non-linear terms is semi-implicit in order to ensure the control of the discrete Cahn-Hilliard free energy. Indeed, a separate study of the pure Cahn-Hilliard system (18)-(19) (i.e. without convective terms, $\mathbf{u}^n = 0$) shows that the discrete free energy control is mandatory to prove the existence of a discrete solution and its convergence towards the solution of the initial problem. If this energy is not controlled, we observed cases where the Newton method does not converge. Different time discretizations for d_i and the analysis of corresponding schemes are given in [6].

In practice, the mobility coefficient M_0^n depends on order parameters at time t^n and is zero outside the interfaces: it is said degenerate. This enables to limit diffusion

outside the interface due to the pure Cahn-Hilliard equations and to keep the spatial localization of the interfaces all along the simulations.

In order to ensure the conservation of the total volume of each constituent, we use the same element for the pressure as for the order parameters and the chemical potentials. Indeed, we have

$$\int_{\Omega} \frac{c_i^{n+1} - c_i^n}{\Delta t} = - \int_{\Omega} \mathbf{u}^n \cdot \nabla c_i^{n+1} = \int_{\Omega} c_i^{n+1} \nabla \cdot \mathbf{u}^n. \quad (23)$$

The last integral is zero thanks to the discrete incompressibility constraint (22) if c_i^{n+1} belongs to the pressure approximation space. In the numerical examples given in Section 4, the velocity is discretized using the \mathbb{Q}_2 element and the other fields using the \mathbb{Q}_1 element.

In (21), the convective terms,

$$\int_{\Omega} \left(\varrho^{n+1} (\mathbf{u}^n \cdot \nabla) \mathbf{u}^{n+1} \right) \cdot \mathbf{v} + \int_{\Omega} \frac{\mathbf{u}^{n+1} \cdot \mathbf{v}}{2} \nabla \cdot (\varrho^{n+1} \mathbf{u}^n),$$

are written under the form

$$\frac{1}{2} \int_{\Omega} \left(\varrho^{n+1} (\mathbf{u}^n \cdot \nabla) \mathbf{u}^{n+1} \right) \cdot \mathbf{v} - \frac{1}{2} \int_{\Omega} \left(\varrho^{n+1} (\mathbf{u}^n \cdot \nabla) \mathbf{v} \right) \cdot \mathbf{u}^{n+1}.$$

In this formulation, the contribution of the convective terms in the kinetic energy balance equation is zero even though the numerical integrations for the finite element method are not exact.

The functions ϱ^{n+1} and η^{n+1} are defined by

$$\begin{aligned} \varrho^{n+1} &= (\varrho_1 - \varrho_3) H_e(c_1^{n+1} - 0.5) + (\varrho_2 - \varrho_3) H_e(c_2^{n+1} - 0.5) + \varrho_3, \\ \eta^{n+1} &= (\eta_1 - \eta_3) H_e(c_1^{n+1} - 0.5) + (\eta_2 - \eta_3) H_e(c_2^{n+1} - 0.5) + \eta_3, \end{aligned} \quad (24)$$

where H_e is a smooth approximation of an Heaviside function. Contrary to the arithmetic or harmonic averages using in the literature, this relation (24) enables to preserve the values ϱ_i and η_i in the phase i even though c_i is not exactly 1 due to numerical errors. Hence, this averaging technique avoids additional numerical errors which appear to be critical in particular when there are large ratios between densities and viscosities of the phases.

3.2 Local adaptive refinement

In the finite element method, basis functions have a small support in comparison to the size of the domain. The idea is to use basis functions with increasingly small support around the smeared interfaces. The basic principle of the CHARMS method is to refine/unrefine primarily basis functions and not directly the cells.

The study of this method and its application to Cahn-Hilliard systems are given in details in [5]. We only recall below the main features of the method.

3.2.1 Adaptation procedure

Consider an initial conforming grid (possibly unstructured) together with its finite elements structure. A conceptual hierarchy of nested grids is defined by successive divisions of cells into cells of the same type obtained by uniformly applying the same subdivision pattern. We obtain a sequence of Lagrange conformal finite element spaces X_j , with the property that each basis function at a given level j can be written as a linear combination of some basis functions of the immediate finer level $j + 1$:

$$X_j \subset X_{j+1} \quad \Rightarrow \quad \varphi_k^j = \sum_l \beta_{k,l}^{j+1} \varphi_l^{j+1},$$

leading to a Child/Parent relationship:

$$\beta_{k,l}^{j+1} \neq 0 \Leftrightarrow \varphi_k^j \text{ is a parent of } \varphi_l^{j+1} \Leftrightarrow \varphi_l^{j+1} \text{ is a child of } \varphi_k^j.$$

Since the supports of basis functions are small, most of the coefficients $\beta_{k,l}^{j+1}$ are zero. Within a set of basis functions, the refinement (resp. unrefinement) of a parent is then defined by the addition (resp. removal) of all its children. Cells are accordingly split and coarsened, leading to nonconforming grids, but their role is limited to be integration domains and support of the basis functions which, more importantly, span conforming finite element spaces.

3.2.2 Time marching and grid construction

For the discrete problem CH/NS proposed in Paragraph 3.1, we use the CHARMS method which involves few modifications in particular for the finite element approximation spaces.

In a time step, from the solution obtained at the previous time t^n , we refine or unrefine the basis functions which belong to \mathcal{V}^n using a given criterion (a criterion for the Cahn-Hilliard/Navier-Stokes applications is given in the following Paragraph 3.2.3). This stage enables to define the new finite element approximation space \mathcal{V}^{n+1} in which we search the solution at time t^{n+1} . The space \mathcal{V}^{n+1} differ, in general, from the approximation space at time t^n . These spaces have not necessarily the same dimensions (the grids are different at each time step).

This method implies that in the variational formulations, some integrals contain basis functions which belong to two distinct approximation spaces \mathcal{V}^{n+1} and \mathcal{V}^n . For example we have to cope with the integral

$$\int_{\Omega} \frac{c_{ih}^n}{\Delta t} \nu^{n+1}, \quad \text{with } c_{ih}^n \in \mathcal{V}^n, \text{ and } \nu^{n+1} \in \mathcal{V}^{n+1}.$$

In order to compute these terms, the grid is built in such a way that each basis function belonging to either \mathcal{V}^n or \mathcal{V}^{n+1} , is expressed as a polynomial function on each cell (the basis function is not piecewise defined on a cell). Thus, if one uses suitable quadrature rules, such integrals are computed exactly. This method in particular avoids the use of intricate transfer operators between the grids.

3.2.3 Refinement/unrefinement criterion

In order to build \mathcal{V}^{n+1} from \mathcal{V}^n , we need to define a refinement/unrefinement criterion. For our applications, we want to refine in the interface zone (that is to say where the order parameters have important variations) and to unrefine away from the interfaces. For this reason, we need to introduce an indicator measuring whether or not a given cell (resp. basis function) lies near the interfaces.

The cell indicator is defined at time t^n by

$$\eta_K = \max\left(\frac{1}{|K|} \int_K c_1^n, \frac{1}{|K|} \int_K c_2^n, \frac{1}{|K|} \int_K c_3^n\right). \quad (25)$$

This cell indicator can be interpreted as follows:

- $\eta_K = 1$ means that the cell K is completely filled with one of the bulk phases.
- $\eta_K < 1$ means that the cell K contains an interface.

Using the cell indicator, we can deduce a criterion for deciding whether or not a given basis function $\varphi \in \mathcal{V}^n$ may be (un-)refined. We use a volume weighted average of η_K over the support of φ :

$$\eta_\varphi = \frac{1}{|\text{supp}[\varphi]|} \sum_{K \cap \text{supp}[\varphi] \neq \emptyset} |K| \eta_K.$$

Given an anticipated cell size $h_{\text{interface}}$ for the interface neighbourhood, the two following criteria let us decide if a basis function φ has to be refined or unrefined:

- Refinement criterion:

$$\eta_\varphi < 0.90 \quad \text{and} \quad \text{diam}(K) > h_{\text{interface}} \quad \text{for at least one cell } K \subset \text{supp}[\varphi].$$

- Unrefinement criterion:

$$\eta_\varphi > 0.95.$$

3.2.4 Summary

The CHARMS method presents some advantages:

- there is no modification of the discrete problem due to the mesh adaptation,
- the possible geometric non-conformity of the adapted meshes are implicitly handled,
- there is no specific treatment due to particular Lagrange finite elements (\mathbb{P}_1 , \mathbb{Q}_1 see Figure 5),
- all the procedure is independent of the space dimension (see Figure 6),
- no need of transfer operators for fields defined on two distinct refined grids.

The use of adaptive local refinement enables us to choose an interface thickness ε very small while conserving a reasonable number of cells as we can see on Figure 7 in the case of a rising gaz bubble (this application is studied in Section 4.2)

4 Applications

In this section, we present two applications: the classical lens spreading between two liquids and the gaz bubble rising in two stratified layers.

The computations are performed in axisymmetric 3D geometry using local adaptive refinement as described above.

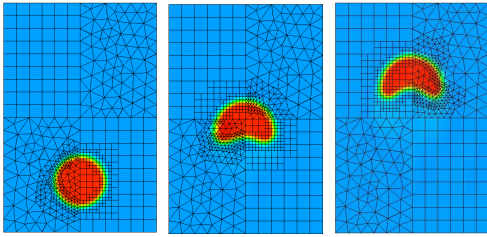


Fig. 5 Use of different finite elements (P_1 and Q_1)

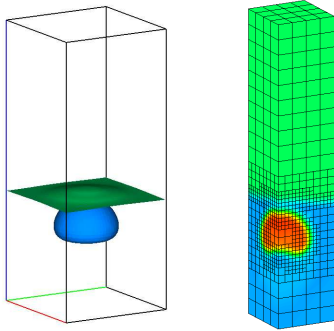


Fig. 6 Example of adaptive local refinement in 3D

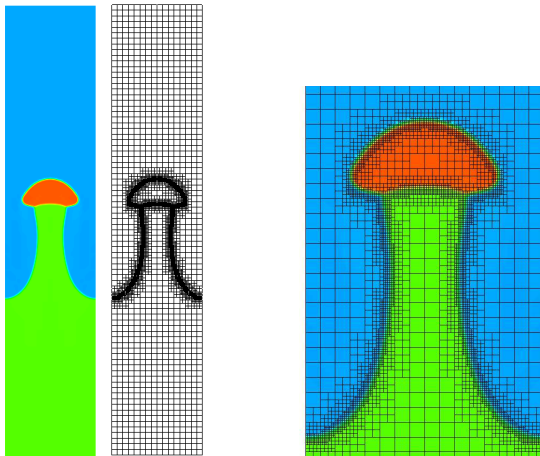


Fig. 7 Rising bubble using local adaptive refinement

4.1 Spreading lens between two stratified layer

In this part, we show that the Cahn-Hilliard/Navier-Stokes model enables to compute accurately contact angles and pressure jumps for the partial spreading of a lens and to simulate the total spreading situation.

4.1.1 Partial spreading - Laplace's law

At equilibrium, the positions of the interfaces are known: the shape of the lens is the intersection of two spherical caps. The contact angles depend on the three surface tensions as given by the Young's relation (see Figure 8).

Young's relation :

$$\frac{\sin \theta_1}{\sigma_{23}} = \frac{\sin \theta_2}{\sigma_{13}} = \frac{\sin \theta_3}{\sigma_{12}}.$$

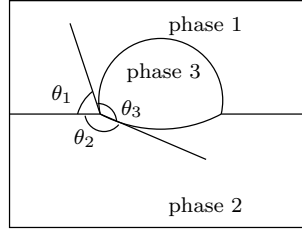


Fig. 8 Shape of the lens at equilibrium

In Figure 9, we present numerical solutions for different surface tension values. The white zone corresponds to the diffuse interface. We obtain a very good agreement with the theoretical solution (black solid line on the figure).

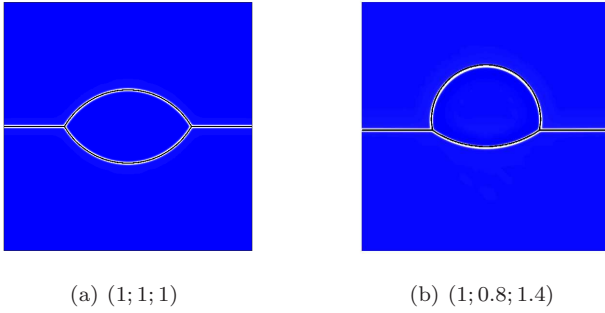


Fig. 9 Equilibrium states obtained numerically for different surface tensions $(\sigma_{12}; \sigma_{13}; \sigma_{23})$

At the equilibrium, if there is no external forces, the theoretical velocity is zero and the pressures are uniform in each phase. The pressure jump between two phases is given by the Laplace's law and is written:

$$p_i - p_j = 2 \frac{\sigma_{ij}}{r_{ij}} \quad (26)$$

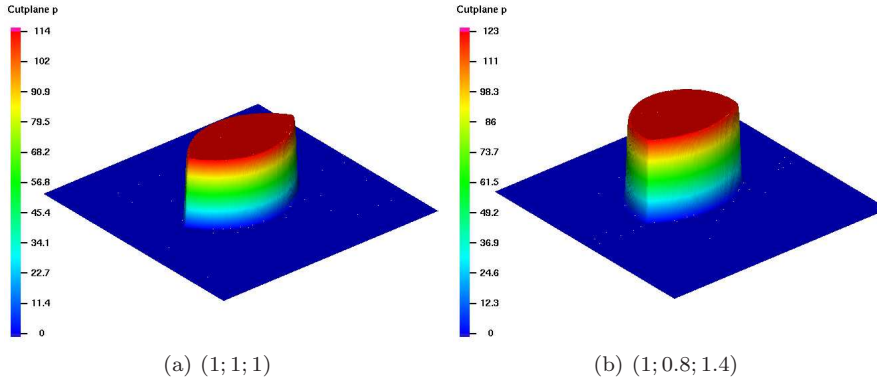
where r_{ij} is the radius of the curvature of the interface between the phases i and j . In this case, the pressures verify:

$$\begin{cases} p_1 = p_2, \\ 2 \frac{\sigma_{13}}{r_{13}} = p_3 - p_1 = p_3 - p_2 = 2 \frac{\sigma_{23}}{r_{23}}. \end{cases} \quad (27)$$

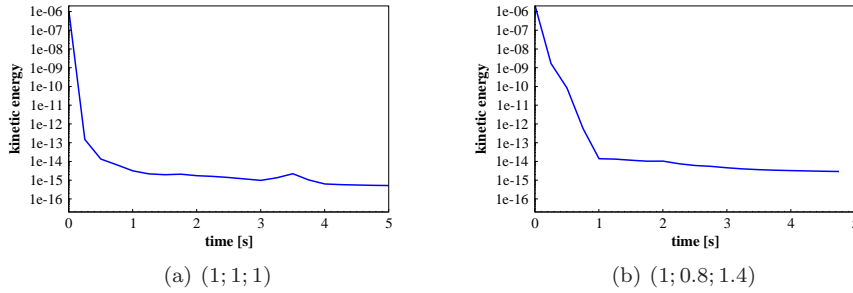
Table 1 Relative error of the pressure jump for different surface tensions

$(\sigma_{12}; \sigma_{13}; \sigma_{23})$	theoretical pressure jump	numerical pressure jump	relative error
(1; 1; 1)	113.101	113.59	0.453%
(1; 0.8; 1.4)	121.644	122.9	1.03%

In Figure 10 and in Table 1, we can see that the Cahn-Hilliard/Navier-Stokes model is able to compute accurately the pressure jump for different surface tensions.

**Fig. 10** Pressure jump for different surface tensions $(\sigma_{12}; \sigma_{13}; \sigma_{23})$

In our computations, the velocity is not zero but very small. We observe parasitic currents which are a common problem for methods where the surface tension force is approximated by a volumic force (see [12]). These spurious currents decrease when the system tends to the equilibrium state. Indeed, in Figure 11, we can see that the kinetic energy decreases during time.

**Fig. 11** Evolution of the kinetic energy for different surface tensions $(\sigma_{12}; \sigma_{13}; \sigma_{23})$

4.1.2 Total spreading

In the case where one of the spreading parameters S_i is positive (that is to say $\Sigma_i < 0$), the spreading is said to be total. Two configurations of total spreading are simulated when the lens spreads between the liquids and when the upper liquid spreads between the lens and the lower liquid. The surface tensions are

- for the lens spreading: $(\sigma_{12}; \sigma_{13}; \sigma_{23}) = (3; 1; 1)$, $\Sigma_3 < 0$,
- for the upper phase spreading: $(\sigma_{12}; \sigma_{13}; \sigma_{23}) = (1; 1; 3)$, $\Sigma_1 < 0$.

We can see on Figure 12 that in both cases, the phase spreads in such a way that the triple points disappear. Then, the system tends to the equilibrium state: the interfaces are finally plane or spherical.

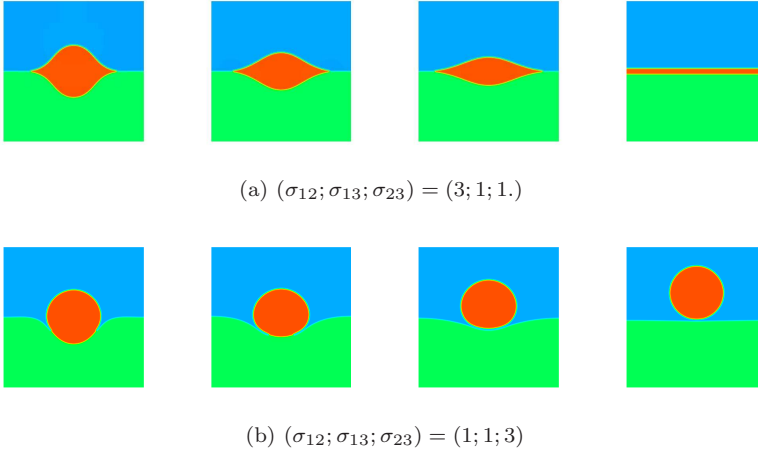


Fig. 12 Evolution of the interface for total spreading situation

4.2 Behaviour of a bubble in stratified two-layers

During a gas bubble rising in a two stratified liquid layers configuration, the bubble can either remain captured in the interface, or can penetrate in the lighter phase leading possibly the heavy phase. In [8, 9], the authors suggest two criteria on the bubble volume to predict the bubble penetration and the entrainment phenomenon. These criteria, based on a macroscopic balance between buoyancy and surface tension forces, have been validated experimentally. The physical parameters we used are given in Table 2. This test case confirms that the model and the numerical method we proposed are able to simulate three-phase flows with large density and viscosity ratios.

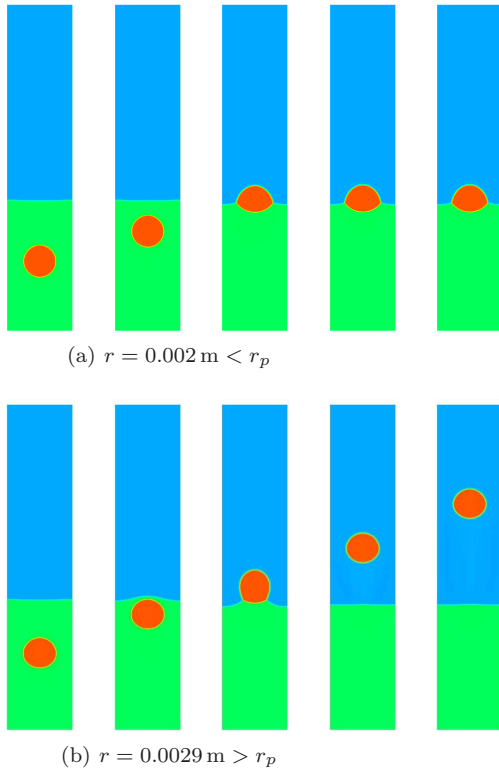
We are interested here in the first criterion which predicts the bubble penetration if its volume V is greater than:

$$V_p = \left(\frac{2\pi \left(\frac{3}{4\pi}\right)^{\frac{1}{3}} \sigma_{23}}{(\rho_3 - \rho_1)g} \right)^{\frac{3}{2}} \simeq 8.87 \cdot 10^{-8} \text{ m}^3,$$

Table 2 Physical properties

surface tension [N.m ⁻¹]			
$\sigma_{\text{gas-liquid}}$	0.07		
$\sigma_{\text{liquid-liquid}}$	0.05		
		density [kg.m ⁻³]	viscosity [Pa.s]
bubble c_1	1		10^{-4}
heavy liquid c_2	1200		0.15
light liquid c_3	1000		0.1

i.e., for a bubble radius greater than $r_p \simeq 2.76 \cdot 10^{-3}$ m. The numerical study gives $r_p^{\text{num}} \simeq 2.5 \cdot 10^{-3}$ m which is in agreement with the criterion (see Figure 13).

**Fig. 13** Bubble rising in two stratified layers.

In the entrainment situations, the authors of [9] studied experimentally the entrained volume of heavy fluid into the light fluid when densities and viscosities vary. We propose to find qualitatively these behaviours computing the quantity of the heavy liquid which is above the initial liquid-liquid interface position. In our study, the simulation with a bubble radius of $r = 8$ mm is considered as the reference case (see Figure

14, circled marks in Figure 15). The physical properties are the same than previously. Our results are in agreement with experiments: we observe an increase of the quantity of entrained volume when the light liquid density increases (see Figure 15(b)) and a decrease of the entrained volume when the viscosities and the heavy liquid density increase (see Figures 15(a), 15(c) and 15(d)).

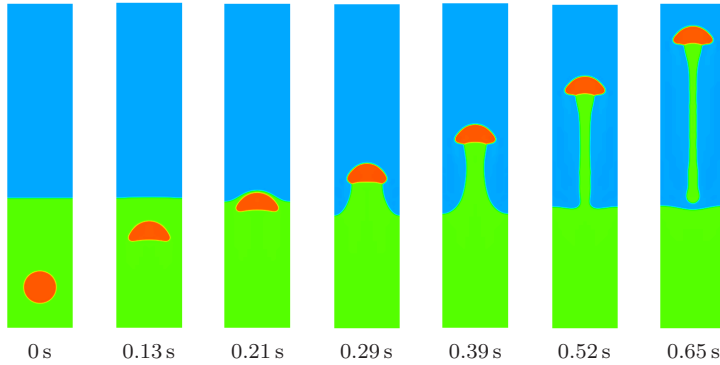


Fig. 14 Entrainment of the heavy liquid during the bubble rising with a radius $r = 8\text{mm}$.

5 Conclusion

In this article, we described a Cahn-Hilliard/Navier-Stokes model for the simulation of incompressible flows composed of three immiscible components, with no phase change. The model is consistent with the two phase model: there is no artificial apparition of the third phase in the interface of the other two. Moreover the model is able to simulate flows with large ratio between the densities and the viscosities, with three different surface tensions and it takes into account total spreading situations.

The local adaptive refinement method enables us to simulate thin interfaces and to have an accurate resolution in the interfacial zone. Finally, in order to compute 3D flows, it is necessary to use efficient linear solvers. In this context, a possible strategy is to use the multi-level structure naturally obtained by the local refinement algorithm in order to build multigrid preconditioners. Such a methodology and corresponding numerical resultat are described in [5].

In further works, we will concentrate on the precise mathematical study of the full numerical method including the coupling between the Cahn-Hilliard and Navier-Stokes equations and the adaptive local refinement method.

References

1. D.M. Anderson, G.B. McFadden. and A.A. Wheeler, Diffuse-Interface Methods in Fluid Mechanics, Annual Review of Fluid Mechanics, 30, 139-165 (1998)
2. T. Bonometti and J. Magnaudet, An interface-capturing method for incompressible two-phase flows. Validation and application to bubble dynamics, International Journal of Multi-phase Flow 33, 109-133 (2007)

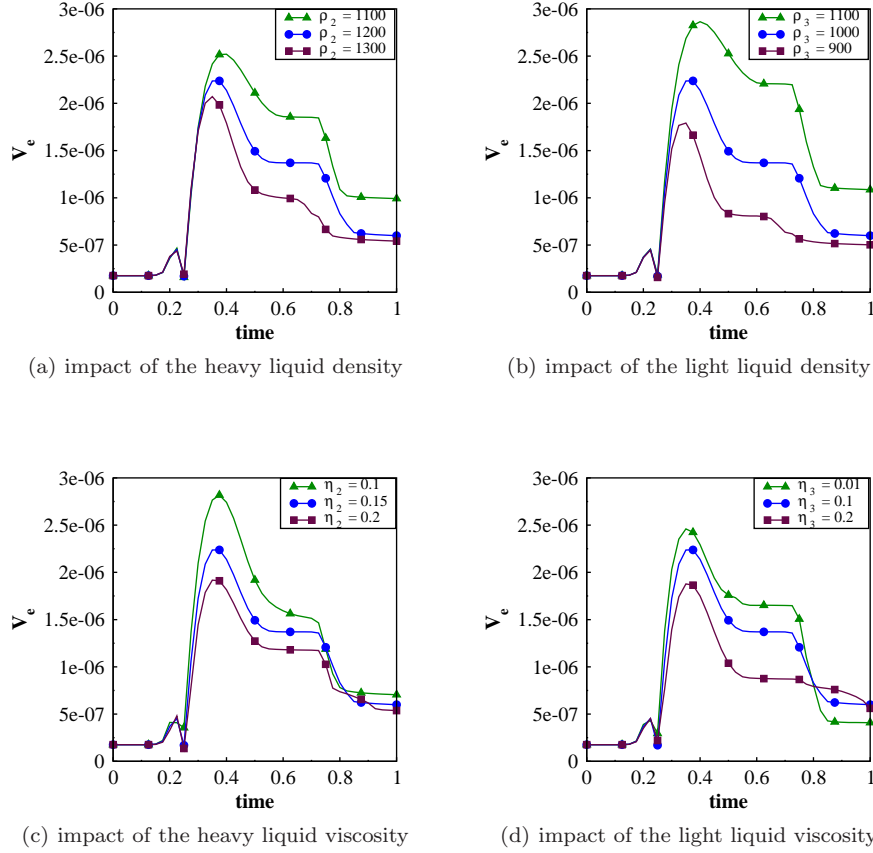


Fig. 15 Evolution of the entrained volume V_e of the heavy liquid in the light liquid

3. F. Boyer, A Theoretical and Numerical Model for the Study of Incompressible Mixture Flows, *Computers and Fluids*, 31, 41-68 (2002)
4. F. Boyer and C. Lapuerta, Study of a three component Cahn-Hilliard flow model, *M2AN Modélisation Mathématique et Analyse Numérique*, 40, 653-687 (2006)
5. F. Boyer, C. Lapuerta, S. Minjeaud and B. Piar, A multigrid method with local adaptive refinement, application to a ternary Cahn-Hilliard model, submitted (2008)
6. F. Boyer and S. Minjeaud, Numerical schemes for a three component Cahn-Hilliard model, in preparation (2008)
7. F. Fichot, P. Meekunnasombat, J. Belloni, F. Duval, A. Garcia and M. Quintard, Two-phase flows in porous media: Prediction of pressure drops using a diffuse interface mathematical description *Nuclear Engineering and Design* 237, 1887-1898 (2007)
8. G.A. Greene, J.C. Chen and M.T. Conlin, Onset of entrainment between immiscible liquid layers due to rising gas bubbles, *International Journal of Heat and Mass Transfer*, 31, 1309-1317 (1988)
9. G.A. Greene, J.C. Chen and M.T. Conlin, Bubble induced entrainment between stratified liquid layers, *International Journal of Heat and Mass Transfer*, 34, 149-157 (1991)
10. J.-L. Guermond and L. Quartapelle, A Projection FEM for Variable Density Incompressible Flows, *Journal of Computational Physics*, 165, 167-188 (2000)
11. D. Jacqmin, Calculation of Two-Phase Navier-Stokes Flows Using Phase-Field Modelling, *Journal of Computational Physics*, 155, 96-127 (1999)

-
12. D. Jamet, D. Torres and J.U. Brackbill, On the Theory and Computation of Surface Tension: The Elimination of Parasitic Currents through Energy Conservation in the Second-Gradient Method, *Journal of Computational Physics*, 182, 262-276 (2002)
 13. A.A. Keller and M. Chen, Effect of Spreading Coefficient on Three-Phase Relative Permeability of NAPL, *Water Resources Research*, 39, 1288 (2003)
 14. J. Kim, A continuous surface tension force formulation for diffuse-interface models, *Journal of Computational Physics*, 204, 784-804 (2005)
 15. J. Kim and J. Lowengrub, Phase field modeling and simulation of three-phase flows, *Interfaces and Free Boundaries*, 7, 435-466 (2005)
 16. J. Kim, Phase field computations for ternary fluid flows, *Computer Methods in Applied Mechanics and Engineering*, 196, 45-48 (2007)
 17. J. Kim, K. Kang and J. Lowengrub, Conservative multigrid methods for ternary Cahn-Hilliard systems, *Communications in Mathematical Sciences*, 2, 53-77 (2004)
 18. P. Krysl, E. Grinspun and P. Schröder, Natural Hierarchical Refinement for Finite Element Methods, *International Journal for Numerical Methods in Engineering*, 56, 1109-1124 (2003)
 19. V. Mani and K.K. Mohanty, Effect of the spreading coefficient on three-phase flow in porous media *Journal of Colloid and Interface Science*, 187, 45-56 (1997)
 20. PELICANS, Collaborative Development environment:
<https://gforge.irsn.fr/gf/project/pelicans/>.
 21. J.S. Rowlinson and B. Widom, *Molecular Theory of Capillarity*. Clarendon Press (1982)
 22. P. Yue, J.J. Feng, C. Liu and J. Shen, A Diffuse-Interface Method for Simulating Two-Phase Flows of Complex Fluids, *Journal of Fluid Mechanics*, 515, 293-317 (2004)